Demonstration of Deuterium's Enhanced Sensitivity to Symmetry Violations Governed by the Standard-Model Extension

A. Nanda,[1,2] D. Comparat,[3] O. Dulieu,[3] S. Lahs,[3,*] C. Malbrunot,[4,5,6] L. Nowak,[1,2] M. C. Simon,[1,†,‡] and E. Widmann[1,‡]

[1]*Stefan Meyer Institute for Subatomic Physics, Dominikanerbastei 16, 1010 Vienna, Austria*
[2]*University of Vienna, Vienna Doctoral School in Physics, Universitätsring 1, Vienna A-1010, Austria*
[3]*Université Paris-Saclay, CNRS, Laboratoire Aimé Cotton, 91405 Orsay, France*
[4]*TRIUMF, 4004 Wesbrook Mall, Vancouver, British Columbia V6T 2A3, Canada*
[5]*Physics Department, McGill University, Montréal, Québec H3A 2T8, Canada*
[6]*Physics and Astronomy, University of British Columbia, Vancouver, British Columbia V6T 1Z1, Canada*

(Received 10 July 2025; revised 20 February 2026; accepted 15 May 2026; published 14 July 2026)

We have performed hyperfine spectroscopy of two transitions in ground-state deuterium and searched for violations of CPT and Lorentz symmetry that would manifest as sidereal variations of the observed transition frequencies. Several nonrelativistic proton coefficients of the Standard-Model extension framework have been addressed. The spin-independent coefficients with momentum power $k = 2$, 4 are constrained for the first time. Bounds on spin-dependent coefficients are improved by exploiting a sensitivity enhancement originating from the relative momenta of the nucleons in the deuteron. The best previous constraints by hydrogen maser measurements are surpassed by 4 and 14 orders of magnitude for coefficients with $k = 2$ and 4, respectively.

DOI: 10.1103/dqvd-15q4

The additional neutron in deuterium (^{2}H; D) with respect to hydrogen (^{1}H; H) leads, on the one hand, to minor changes of molecular bonds and to small isotope shifts [1]. On the other hand, the masses of the two isotopes (relevant to metrology and neutrino physics [2]), their synthesis in the early Universe (indicator for cosmological parameters [3]), and their hyperfine structure [4] are quite distinct. Consequently, there are compelling reasons for both comparative and complementary studies. Those also extend to exotic versions of H and D, where the electron is replaced by a muon [5–9], pion [10,11], kaon [12–14], or antiproton [15–19]. Such experiments gave rise to the proton and deuteron radii puzzles and probed quantum chromodynamics at low energies, thereby challenging and advancing the standard model (SM) of particle physics. H masers were employed in high precision measurements to test beyond SM physics [20,21] and, more recently, isotope shifts were recognized as a tool for placing bounds on new light-mass bosons [22].

Here, we exploit another significant difference between the two isotopes: the proton momentum $\boldsymbol{p}$ from internal nuclear motion is by far higher in D ($\sim$0.1 GeV/c) than in H ($\sim$1 keV/c). As noted by Kostelecký and Vargas a decade ago [23] and elaborated for the present measurement lately [24], this results in orders of magnitude higher sensitivity to specific violations of CPT (combination of three discrete symmetries: Charge conjugation, parity, and time reversal) and Lorentz symmetry. Accordingly, we report on Rabi-type measurements [25] of two hyperfine transitions in ground-state D and search for sidereal variations of the frequency signals in order to extract new and improved constraints within the Standard-Model extension (SME) framework [26–28].

The nuclear spin quantum number of D equals one. Therefore, the ground-state hyperfine structure consists of a doublet and a quadruplet with corresponding total angular momentum quantum number F of $\frac{1}{2}$ and $\frac{3}{2}$, respectively. In the presence of an external magnetic field (B_{stat}), the degeneracy is lifted by different Zeeman shifts as described by the Breit-Rabi formula [4,29] and shown in Fig. 1. We investigate the two transitions with $\Delta M_F = 0$: σ_1 (F, M_F: $\frac{3}{2}, \frac{1}{2} \to \frac{1}{2}, \frac{1}{2}$) and σ_2 (F, M_F: $\frac{3}{2}, -\frac{1}{2} \to \frac{1}{2}, -\frac{1}{2}$), where M_F is the magnetic quantum number. The magnetic field dependence of these transition frequencies reads

*Present address: Vienna Center for Quantum Science and Technology, Atominstitut, TU Wien 1020, Vienna, Austria.
†Contact author: martin.simon@oeaw.ac.at
‡Present address: Marietta Blau Institute for Particle Physics, Dominikanerbastei 16, 1010 Vienna, Austria.

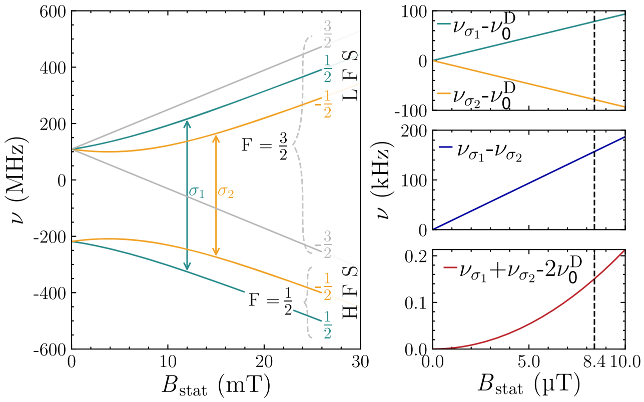

FIG. 1. (Left) Breit-Rabi diagram of deuterium showing the ground-state hyperfine structure and Zeeman shifts. The two σ transitions ($\Delta M_F = 0$) are indicated with arrows and connect low-field-seeking (LFS) states of the quadruplet ($F = \frac{3}{2}; M_F = -\frac{3}{2}, -\frac{1}{2}, \frac{1}{2}, \frac{3}{2}$) with high-field-seeking (HFS) states of the doublet ($F = \frac{1}{2}; M_F = -\frac{1}{2}, \frac{1}{2}$). (right) Close-up views into the low magnetic field range relevant for this Letter ($B_{\text{stat}} = 8.4$ μT, dashed line) show the Zeeman shifts for the σ transitions as well as their combinations as difference and sum frequencies $\nu_\pm = \nu_{\sigma_1} \pm \nu_{\sigma_2}$.

$$\nu_{\sigma_1} = \nu_0^{\text{D}} \sqrt{1 + \frac{2}{3}x + x^2}, \quad \nu_{\sigma_2} = \nu_0^{\text{D}} \sqrt{1 - \frac{2}{3}x + x^2}, \quad (1)$$

with $\nu_0^{\text{D}} = 327\,384\,352.5222(17)$ Hz [30] the zero-field hyperfine splitting and $x = \mu_-^{\text{D}} B_{\text{stat}}/(h\nu_0^{\text{D}})$, where h is Planck's constant and $\mu_-^{\text{D}} = -g_{\text{e}}\mu_{\text{B}} - g_{\text{d}}\mu_{\text{N}}$. Here, μ_{B} (μ_{N}) and g_{e} (g_{d}) are the Bohr (nuclear) magneton and the electron (deuteron) g factor, respectively. We use 2022 CODATA values [31], where the sign of g_{e} is negative. The field of $B_{\text{stat}} = 8.4$ μT applied in this Letter corresponds to $x \simeq 7 \times 10^{-4}$.

The aforementioned SME framework generalizes the SM Lagrangian by adding operators violating Lorentz and *CPT* symmetry. Each operator of mass dimension d is introduced with an associated coefficient of matching mass dimension $4 - d$, and effects on observables, such as shifts of transition frequencies, can be calculated. Thus, the SME enables quantitative comparability of various experiments contributing to a comprehensive and systematic search for symmetry violations [32]. Its initial minimal version [26–28] included Lorentz-violating operators with $d \leq 4$ and has been extended to incorporate arbitrary d within the nonminimal SME [33–35]. Combinations of coefficients for the same particle (i.e., flavor w like proton p, neutron n, or electron e), including those with different d, tend to appear together in calculations of observable effects and are conveniently collected as effective coefficients. The example of relevance for the present Letter are the spherical nonrelativistic (NR) coefficients, where two types are distinguished:

$$\begin{aligned} \text{spin-dependent:}\ \mathcal{T}_{w_{kjm}}^{\text{NR}(qP)} &= g_{w_{kjm}}^{\text{NR}(qP)} - H_{w_{kjm}}^{\text{NR}(qP)}, \\ \text{spin-independent:}\ \mathcal{V}_{w_{kjm}}^{\text{NR}} &= c_{w_{kjm}}^{\text{NR}} - a_{w_{kjm}}^{\text{NR}}, \end{aligned} \quad (2)$$

with decompositions into *CPT*-odd (g, a) and *CPT*-even (H, c) contributions. Here, the index k gives the momentum power, while j and m are the spherical tensor rank and component. In brackets the spin weight q and parity type P of the operators are indicated, where parity types are denoted as the E and B-type for $(-1)^j$ and $(-1)^{j-1}$, respectively. In this Letter the combinations $(0B)$ and $(1B)$ for spin-dependent and $(0E)$ for spin-independent coefficients appear.

In principle, the present experiment on D tests e, n, and p coefficients. However, for e coefficients, D gives no advantage over H, as the electron's relative momenta are basically identical. Furthermore, stringent constraints for n coefficients exist from comagnetometry experiments, summarized in Table VI of Ref. [36]. Therefore, we concentrate on the subset of nonminimal NR p coefficients, where comagnetometry could not provide constraints yet, due to the lack of sufficiently elaborate nuclear structure modeling (see discussion in the End Matter). The relationships between these coefficients and the energy shifts of the σ transition are given by Eq. (19) of Ref. [24]. By forming their difference and sum ($\delta\nu_\pm = \delta\nu_{\sigma_1} \pm \delta\nu_{\sigma_2}$) the relations separate into spin-dependent and spin-independent components. In natural units (speed of light and reduced Planck constant set to one: $c = \hbar = 1$) we obtain

$$\begin{aligned} 2\pi\,\delta\nu_- &= \frac{1}{6\sqrt{3\pi}} \sum_{\substack{k=0,2,4\\ q=0,1}} (-1)^q \langle |\boldsymbol{p}|^k \rangle_{(qB)} \mathcal{T}_{p_{k10}}^{\text{NR}(qB)}, \\ 2\pi\,\delta\nu_+ &= -\frac{1}{2\sqrt{5\pi}} \sum_{k=2,4} \langle |\boldsymbol{p}|^k \rangle_{(0E)} \mathcal{V}_{p_{k20}}^{\text{NR}}, \end{aligned} \quad (3)$$

where $\langle |\boldsymbol{p}|^k \rangle_{(qP)}$ are the momentum expectation values of order k. For $k = 2, 4$, those are orders of magnitude larger in D than in H [24], and thus the source of the sensitivity enhancement exploited in this Letter.

In the inertial reference frame of the Sun, the SME coefficients are constant [32]. Their transformation to the coefficients acting in the Earth's frame is expressed by Eq. (22) of Ref. [24]. Concentrating on the terms relevant to this Letter we can reduce Eq. (25) of Ref. [24] to

$$\begin{aligned} \mathcal{T}_{p_{k10}}^{\text{NR}(qB)} &= -\sqrt{2}\sin\vartheta\,\Re\left(e^{i\omega_\oplus T_L}\mathcal{T}_{p_{k11}}^{\text{NR}(qB),\text{Sun}}\right), \\ \mathcal{V}_{p_{k20}}^{\text{NR}} &= -\sqrt{\frac{3}{2}}\sin 2\vartheta\,\Re\left(e^{i\omega_\oplus T_L}\mathcal{V}_{p_{k21}}^{\text{NR,Sun}}\right) \\ &\quad + \sqrt{\frac{3}{2}}\sin^2\vartheta\,\Re\left(e^{i2\omega_\oplus T_L}\mathcal{V}_{p_{k22}}^{\text{NR,Sun}}\right), \end{aligned} \quad (4)$$

where ϑ is the angle between the aligning static magnetic field $B_{\rm stat}$ and the Earth's rotation axis, $\omega_\oplus \simeq 2\pi/$ (23 h 56 min) is the sidereal frequency, and T_L is the local sidereal time [24] defined such that the argument in the complex exponent can be written without constant phase offset. The real ($\Re$) and imaginary ($\Im$) part of the coefficients in the Sun-centered frame would induce variations on the related coefficient in the Earth's frame following $\cos(m\omega_\oplus T_L)$ and $\sin(m\omega_\oplus T_L)$ functions, respectively.

A Rabi-type H beamline has been constructed by the ASACUSA Collaboration to characterize equipment for antihydrogen hyperfine spectroscopy [37–39]. It was optimized for H velocities of $v_{\rm H} \simeq 1000\ {\rm ms}^{-1}$, as this matched the anticipated antihydrogen beam properties. Upgrades to the initial apparatus, like combinations of ring apertures and sextupole magnets, which select narrow velocity ranges ($\Delta v_{\rm H} \lesssim 40\ {\rm ms}^{-1}$), are succinctly described in [40,41].

In the present Letter, we employ the existing source and detector. The generation of a cold, modulated, and polarized atomic D beam merely requires supplying D_2 gas (instead of H_2), and for the detection, the quadrupole mass spectrometer selects a mass of 2 amu (instead of 1 amu). The beam temperature and magnetic gradient force remain the same. The corresponding scaling of velocities ($v_{\rm D} \simeq 700\ {\rm ms}^{-1}$) and accelerations due to the mass difference between atomic H and D results in trajectories which are basically identical for both species.

The cavity assembly, however, had to be replaced entirely. As sketched in Fig. 2, it consists of a vacuum chamber housing a radio-frequency (rf) resonator surrounded by a solenoid and a cylindrical three-layer magnetic shielding [41]. The resonator employs a split ring geometry [43] to provide the oscillating magnetic field $B_{\rm osc}$ around the frequency of $\nu_0^{\rm D}$ for stimulation of the hyperfine transitions. Elongated versions of such resonators produce homogeneous axial oscillating magnetic fields within the inner cylindrical volume. A distinctive feature of our device is a second gap, making it a double-gap split ring resonator (DSRR) [46,47]. Gap size changes for frequency tuning are more flexible and avoid mechanical tension. A signal generator connected to an in-phase power divider supplies two rf waves. Those pass a weak, capacitive, over-coupled link and get fed into each shell of the DSRR from opposite ends through direct electrical contacts. Coaxial to the feeding pin a pick-up antenna coupled to a spectrum analyzer monitors the rf field built up in the resonator. The rf devices are locked to an external 10 MHz signal with 10^{-14} relative uncertainty, which is derived from the metrological network REFIMEVE [48–50].

Inside the magnetic shielding layers, the solenoid with 630 mm in length and 170 mm inner diameter generates $B_{\rm stat}$. Compensation turns counteract the field drop at the entrance and exit of the solenoid. Field mappings within the

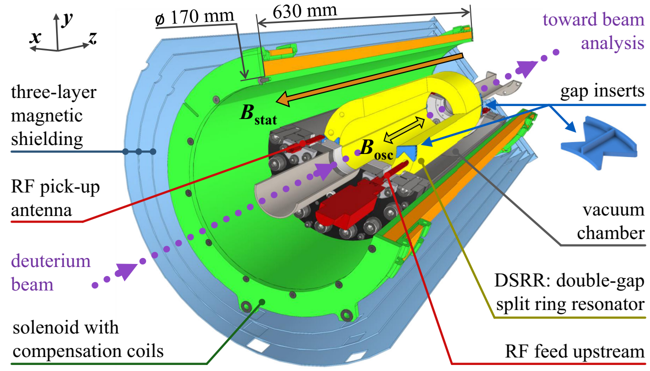

FIG. 2. Sketch of the purpose-built cavity assembly. The static and oscillating magnetic fields ($\boldsymbol{B}_{\rm stat}\|\boldsymbol{B}_{\rm osc}$) needed to induce the σ hyperfine transitions in D are indicated by the long arrow and short double-arrow, respectively. A solenoid with compensation coils in a three-layer magnetic shielding generates $\boldsymbol{B}_{\rm stat}$. A double-gap split ring resonator in a vacuum enclosure provides $\boldsymbol{B}_{\rm osc}$. Length and inner diameter dimensions are given for the main solenoid. By variation of the gap size through 3D-printed polymeric gap inserts the resonance frequency of the device was tuned to be close to $\nu_0^{\rm D}$.

interaction volume at ~200 μT [41] using fluxgate sensors confirmed values for the field inhomogeneity of $\varsigma_B/\bar{B} \simeq 5\times 10^{-4}$, where ς_B refers to the standard deviation of the measured field values and overlines are used to denote averages from here on. Currents are monitored as a proxy for the generated static field. Fluxgate sensors provide direct magnetic field measurements inside and outside of the magnetic shielding. Seven temperature sensors are mounted at critical positions to verify environmental stability.

The polarized D beam entering the interaction region consists of equal parts of the three LFS states (see Fig. 1). Depending on the rf settings, a fraction of one of these states converts to a HFS state. Prior to detection those atoms get removed from the beam by magnetic field gradients. The signature for a resonant interaction is thus a drop in count rate, which at best can amount to one-third of the total beam rate.

Rabi oscillations were observed by setting the frequency to the center of a transition and scanning the rf power. The first state population inversion corresponds to a π pulse. Supplied rf powers of −9.4 and −10.1 dBm were found to be optimal for σ_1 and σ_2 transitions, respectively. At these power settings, the frequency scans were performed.

The acquisition of a *resonance pair* consisted of pointwise interleaved scans of the σ_1 and σ_2 transition beam rates (R_σ), each sampled in a randomized sequence of 25 frequency points separated by 500 Hz. Prior to and following each R_σ, a reference measurement without rf interaction was performed ($R_{\rm ref}$). This enabled converting rates into probabilities through: $\mathcal{P} = 1 - R_\sigma/R_{\rm ref}$ [41].

Two campaigns of about one week duration each have been conducted in May (No. 1) and August (No. 2) 2023,

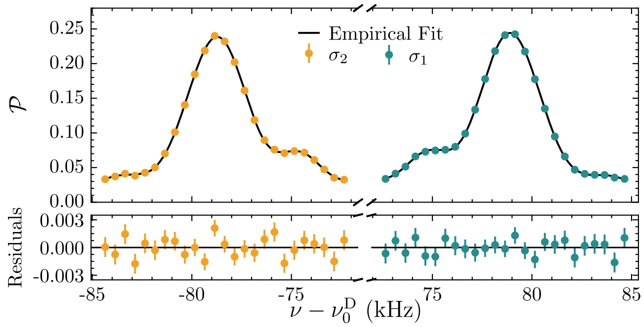

FIG. 3. High-statistic transition probability spectra for the σ_1 (right) and σ_2 (left) transition by averaging all 107 resonance pairs of campaign No. 2. The asymmetries originate from small inhomogeneities of B_{stat}. The two transitions feature a mirrored line shape due to their opposite Zeeman shifts. The line shows an empirical fit with 9 parameters, which is then used like a template to fit every resonance individually with only 3 free fit parameters. Uncertainties are smaller than the dots and hence visualized as residuals in the lower panel.

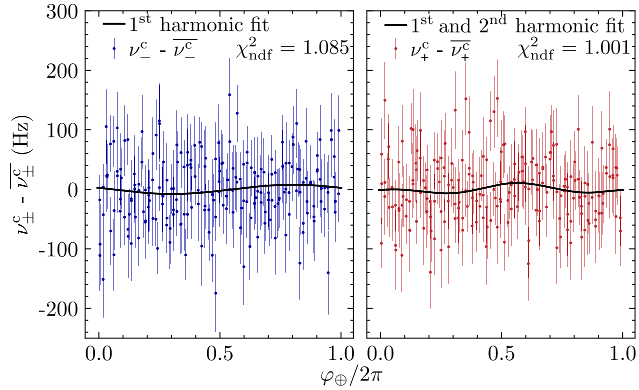

FIG. 4. The difference and sum frequencies with offset corrections by subtracting averages ($\nu_\pm^c - \overline{\nu_\pm^c}$) (for details see End Matter) are plotted against the sidereal phase in the top graphs. A fit (black line), according to Eq. (5), extracts the values and statistical uncertainties of the amplitudes.

accumulating 106 and 107 resonance pairs, respectively. High-statistic probability spectra for both transitions are obtained by adding up all data of a campaign, as exemplified in Fig. 3. The observed asymmetry is attributed to small inhomogeneities of B_{stat} and is mirrored between the σ_1 and σ_2 transitions due to the opposite Zeeman shifts. The high-statistic spectra are used to *predetermine* 6 parameters of an empirical fit function with 9 parameters in total (see End Matter for details). When applied to the individual resonance pairs only 3 fit parameters are free, namely, a linear scaling of the function to the observed probabilities (two parameters) and the central frequency ν^c.

Searches for sidereal variations are performed on the combined frequencies $\nu_\pm^c = \nu_{\sigma_1}^c \pm \nu_{\sigma_2}^c$ by plotting them against the mean sidereal phase $\varphi_\oplus = \mathrm{mod}\,(\omega_\oplus T_L, 2\pi)$ of the data taking period for the corresponding resonance pair. Several amplitudes get extracted by fitting:

$$\delta\nu_\pm(\varphi_\oplus) = A_0^\pm + C_1^\pm \cos\varphi_\oplus + S_1^\pm \sin\varphi_\oplus + C_2^+ \cos 2\varphi_\oplus + S_2^+ \sin 2\varphi_\oplus. \tag{5}$$

Amplitudes for variations at the second harmonic are only relevant for $\mathcal{V}$ coefficients. Therefore, those are only extracted from the sum frequencies ν_+^c. Figure 4 displays these fits on the data of both campaigns. The constant $A_0^\pm$ is removed by subtracting averages of the frequencies ($\overline{\nu_\pm^c}$), which are formed separately for three uninterrupted data taking periods (see End Matter for details on this *offset correction*).

A relation between the SME coefficients in the Sun-centered frame and the amplitudes of sidereal variations of the hyperfine transitions measured in the Earth's frame is obtained by combining Eqs. (3)–(5). Introducing a complex-valued amplitude $\mathcal{A}_m^\pm = C_m^\pm - iS_m^\pm$ and using natural units, we obtain

$$2\pi\,\mathcal{A}_1^- = -\frac{\sin\vartheta}{3\sqrt{6\pi}} \sum_{\substack{k=0,2,4\\ q=0,1}} (-1)^q \langle|\boldsymbol{p}|^k\rangle_{(qB)} \mathcal{T}_{p_{k11}}^{\mathrm{NR}(qB),\mathrm{Sun}},$$

$$2\pi\,\mathcal{A}_1^+ = \frac{\sin 2\vartheta}{2}\sqrt{\frac{3}{10\pi}} \sum_{k=2,4} \langle|\boldsymbol{p}|^k\rangle_{(0E)} \mathcal{V}_{p_{k21}}^{\mathrm{NR,Sun}},$$

$$2\pi\,\mathcal{A}_2^+ = -\frac{\sin^2\vartheta}{2}\sqrt{\frac{3}{10\pi}} \sum_{k=2,4} \langle|\boldsymbol{p}|^k\rangle_{(0E)} \mathcal{V}_{p_{k22}}^{\mathrm{NR,Sun}}. \tag{6}$$

Note that the only complex-valued contributions on the right-hand sides are the SME coefficients. The experiment was performed at the Laboratoire Aimé Cotton in Orsay near Paris at a latitude of $48.7072 \pm 0.0002°$. B_{stat} is oriented $6 \pm 2°$ anticlockwise from due south when viewed from above, hence, $\vartheta = 131.02 \pm 0.18°$ [51].

Systematic investigations evaluated various correlations between central frequencies ν^c extracted by the fits, rf power monitoring, temperatures, direct and indirect magnetic field measurements, as well as variations of the six predetermined parameters by 3 standard deviations of the empirical fit function and extraction of the linear independent amplitudes by fitting every term of Eq. (5) separately to the data instead of simultaneously, as shown in Fig. 4. However, all those tests showed negligible effects at the present level of statistics. A search for other frequency components confirmed the absence of any significant signal in a wider range (see End Matter for details). The impact of the aforementioned *offset correction* was tested by rerunning the analysis without distinguishing uninterrupted data taking periods. The absolute difference between the complex amplitudes $\mathcal{A}$ obtained with these two methods serves as a measure for systematic effects. Amplitudes from the frequency difference ($\mathcal{A}^-$) appeared more susceptible to systematic effects than those of the sum frequency ($\mathcal{A}^+$),

TABLE I. Values with statistical, total, and systematic uncertainties (1 std. dev.) for the amplitudes in units of Hz extracted by fits according to Eq. (5), as shown in Fig. 4.

Ampl. (Hz)	$C_m^\pm = \Re(\mathcal{A}_m^\pm)$			$S_m^\pm = -\Im(\mathcal{A}_m^\pm)$			Common
$\pm$, harm.	Value	Stat.	Tot.	Value	Stat.	Tot.	Syst.
$\mathcal{A}_1^-$	2.5	5.0	6.2	−7.4	4.9	6.1	3.7
$\mathcal{A}_1^+$	−4.7	5.0	5.1	−2.7	4.9	5.0	1.2
$\mathcal{A}_2^+$	3.8	4.9	4.9	3.7	4.9	4.9	0.3

which is reasonable as the first order Zeeman shifts cancel for the latter. All values and uncertainties of amplitudes are summarized in Table I, with the last column showing the potential systematic effects stemming from the offset correction, which is smaller than statistical uncertainties.

All constraints on SME coefficients derived from the amplitude limits are summarized in Table II. Details are exemplified and listed in [41]. The spin-dependent coefficients $\mathcal{T}_{p_{kjm}}^{\mathrm{NR}(qP)}$ of momentum power $k = 0$ are better constrained by H maser measurements [20,21,23], while those for $k = 2$ and 4 are improved by 4 and 14 orders of magnitude. This significant improvement can be entirely attributed to the use of D, taking advantage of the substantially larger proton momentum compared to H, while it is still a similarly well-calculable system. The spin-independent coefficients $\mathcal{V}_{p_{kjm}}^{\mathrm{NR}}$ are constrained for the first time.

In summary, we have provided improved as well as new constraints on CPT and Lorentz symmetry violations governed by nonrelativistic proton coefficients of the SME framework by searching for sidereal variations in combined frequencies of the σ_1 and σ_2 transition of the D ground-state hyperfine structure. Despite inferior absolute precision in comparison to H maser measurements, an improvement was possible due to a strong sensitivity enhancement mediated by the proton's momentum in the deuteron, thereby highlighting the potential of complementing D studies.

With further campaigns, the D experiment could provide additional constraints through a boost analysis as discussed in [24]. Other opportunities are opened by measurements at various static magnetic field values and especially by reversing the field direction to address those SME coefficients, which do not lead to sidereal variations as showcased for H just recently [40]. Operation at lower velocities [52,53] in the existing setup, introducing the Ramsey method [54–56] in an improved setup, or a dedicated D maser [30] could provide sensitivity enhancements of about 1, 2, or 3 orders of magnitude, respectively.

Finally, the community at the antiproton decelerator and extra low energy antiproton ring facility (AD-ELENA) of CERN is presently evaluating future opportunities offered by antideuterons. Beyond the more general possibility of comparative antimatter studies to decouple limits on CPT-even and CPT-odd coefficients, this system could give unique access to antineutron properties.

TABLE II. Constraints on CPT-even (H, c) and CPT-odd (g, a) nonminimal NR SME proton coefficients in the Sun-centered frame as values with total uncertainties: (top section) For spin-dependent coefficients of momentum power $k = 2, 4$ the enhanced sensitivity of D enables significantly stronger constraints than achieved in H maser measurements. (bottom section) Spin-independent coefficients are constrained for the first time through the sum frequency ν_+.

Spin-depend. coeff.	$\Re(\mathcal{T}^{\mathrm{Sun}})$	$\Im(\mathcal{T}^{\mathrm{Sun}})$	Units
$H_{p_{211}}^{\mathrm{NR(0B)}}, -g_{p_{211}}^{\mathrm{NR(0B)}}$	0.6 ± 1.6	1.9 ± 1.6	10^{-20} GeV^{-1}
$H_{p_{211}}^{\mathrm{NR(1B)}}, -g_{p_{211}}^{\mathrm{NR(1B)}}$	1.5 ± 3.7	4.4 ± 3.6	10^{-20} GeV^{-1}
$H_{p_{411}}^{\mathrm{NR(0B)}}, -g_{p_{411}}^{\mathrm{NR(0B)}}$	1.8 ± 4.6	5.4 ± 4.5	10^{-20} GeV^{-3}
$H_{p_{411}}^{\mathrm{NR(1B)}}, -g_{p_{411}}^{\mathrm{NR(1B)}}$	-0.5 ± 1.1	-1.4 ± 1.1	10^{-19} GeV^{-3}
Spin-independ. coeff.	$\Re(\mathcal{V}^{\mathrm{Sun}})$	$\Im(\mathcal{V}^{\mathrm{Sun}})$	**Units**
$c_{p_{221}}^{\mathrm{NR}}, -a_{p_{221}}^{\mathrm{NR}}$	1.6 ± 1.8	-0.9 ± 1.7	10^{-20} GeV^{-1}
$c_{p_{222}}^{\mathrm{NR}}, -a_{p_{222}}^{\mathrm{NR}}$	-2.3 ± 3.0	2.2 ± 3.0	10^{-20} GeV^{-1}
$c_{p_{421}}^{\mathrm{NR}}, -a_{p_{421}}^{\mathrm{NR}}$	-0.9 ± 1.0	0.5 ± 1.0	10^{-19} GeV^{-3}
$c_{p_{422}}^{\mathrm{NR}}, -a_{p_{422}}^{\mathrm{NR}}$	1.3 ± 1.7	-1.2 ± 1.7	10^{-19} GeV^{-3}

Acknowledgments—We would like to express our gratitude to Arnaldo Vargas for laying the theoretical foundations this work is based on and for numerous enlightening discussions on the SME, to the staff of the SMI Advanced Instrumentation group for hardware support, to the technological platform of LAC (LAC Tech'), in particular, Christophe Siour, for contributions to the transport of the experiment from CERN and its reinstallation at LAC, as well as to Simon Rheinfrank for valuable measurements on the static magnetic and rf fields. We thank CERN's technical service groups for their continued support in general and specifically Manfred Wendt and the late Fritz Caspers for sharing their rf expertise, as well as Maxime Dumas, Luke Von Freeden, Mikko Karppinen, and the late Roberto Lopez for assisting our solenoid design. This project is supported by the European Union's Horizon 2020 research and innovation program under the Marie Skłodowska-Curie Grant Agreement No. 721559, the Austrian Science Fund FWF, Doctoral Program No. W1252-N27, and the TRIUMF start-up fund (Canada). We acknowledge funding by the Austrian Academy of Sciences through the Investment Initiative. This work was supported by program "Investissements d'Avenir" launched by the French Government and implemented by ANR with the references ANR-21-ESRE-0029 [ESR/Equipex + T-REFIMEVE and No. ANR-10-IDEX-0001-002 PSL (PSL)]. Support from the CPER project COMB'IdF (Convention No. 2022-IDF-P2 of Ministère de l'Enseignement Supérieur, de la Recherche et de l'Innovation, and of Région Ile-de-France) is gratefully acknowledged.

Data availability—The data that support the findings of this article are not publicly available upon publication because it is not technically feasible and/or the cost of preparing, depositing, and hosting the data would be prohibitive within the terms of this research project. The data are available from the authors upon reasonable request.

[1] K. Pachucki, M. Weitz, and T. W. Hänsch, Theory of the hydrogen-deuterium isotope shift, Phys. Rev. A **49**, 2255 (1994).

[2] S. Rau, F. Heiße, F. Köhler-Langes, S. Sasidharan, R. Haas, D. Renisch, C. E. Düllmann, W. Quint, S. Sturm, and K. Blaum, Penning trap mass measurements of the deuteron and the HD+ molecular ion, Nature (London) **585**, 43 (2020).

[3] V. Mossa, K. Stöckel, F. Cavanna, F. Ferraro, M. Aliotta, F. Barile, D. Bemmerer, A. Best, A. Boeltzig, C. Broggini *et al.*, The baryon density of the universe from an improved rate of deuterium Burning, Nature (London) **587**, 210 (2020).

[4] J. E. Nafe and E. B. Nelson, The hyperfine structure of hydrogen and deuterium, Phys. Rev. **73**, 718 (1948).

[5] R. Pohl, A. Antognini, F. Nez, F. D. Amaro, F. Biraben, J. M. R. Cardoso, D. S. Covita, A. Dax, S. Dhawan, L. M. P. Fernandes *et al.*, The size of the proton, Nature (London) **466**, 213 (2010).

[6] A. Antognini, F. Nez, K. Schuhmann, F. D. Amaro, F. Biraben, J. M. R. Cardoso, D. S. Covita, A. Dax, S. Dhawan, M. Diepold *et al.*, Proton structure from the measurement of 2S-2P transition frequencies of muonic hydrogen, Science **339**, 417 (2013).

[7] R. Pohl, F. Nez, L. M. P. Fernandes, F. D. Amaro, F. Biraben, J. M. R. Cardoso, D. S. Covita, A. Dax, S. Dhawan, M. Diepold *et al.*, Laser spectroscopy of muonic Deuterium, Science **353**, 669 (2016).

[8] H. Gao and M. Vanderhaeghen, The proton charge radius, Rev. Mod. Phys. **94**, 015002 (2022).

[9] O. Hernandez, A. Ekström, N. Nevo Dinur, C. Ji, S. Bacca, and N. Barnea, The deuteron-radius puzzle is alive: A new analysis of nuclear structure uncertainties, Phys. Lett. B **778**, 377 (2018).

[10] D. Gotta, Precision spectroscopy of light exotic atoms, Prog. Part. Nucl. Phys. **52**, 133 (2004).

[11] T. Strauch, F. D. Amaro, D. F. Anagnostopoulos, P. Bühler, D. S. Covita, H. Gorke, D. Gotta, A. Gruber, A. Hirtl, P. Indelicato *et al.*, Precision determination of the $d\pi \leftrightarrow$ nn transition strength at threshold, Phys. Rev. Lett. **104**, 142503 (2010).

[12] M. Iwasaki, R. S. Hayano, T. M. Ito, S. N. Nakamura, T. P. Terada, D. R. Gill, L. Lee, A. Olin, M. Salomon, S. Yen *et al.*, Observation of kaonic hydrogen $K\alpha$ x rays, Phys. Rev. Lett. **78**, 3067 (1997).

[13] G. Beer, A. M. Bragadireanu, M. Cargnelli, C. Curceanu-Petrascu, J.-P. Egger, H. Fuhrmann, C. Guaraldo, M. Iliescu, T. Ishiwatari, K. Itahashi *et al.*, Measurement of the kaonic hydrogen x-ray spectrum, Phys. Rev. Lett. **94**, 212302 (2005).

[14] C. Curceanu, C. Guaraldo, M. Iliescu, M. Cargnelli, R. Hayano, J. Marton, J. Zmeskal, T. Ishiwatari, M. Iwasaki, S. Okada *et al.*, The modern era of light kaonic Atom experiments, Rev. Mod. Phys. **91**, 025006 (2019).

[15] J. Richard and M. Sainio, Nuclear effects in protonium, Phys. Lett. B **110**, 349 (1982).

[16] S. Wycech, A. Green, and J. Niskanen, On the energy levels in antiprotonic deuterium, Phys. Lett. B **152**, 308 (1985).

[17] C. Baker, C. Batty, S. Clark, J. Moir, S. Sakamoto, J. Davies, J. Lowe, J. Nelson, G. Pyle, A. Selvarajah *et al.*, Measurement of x-rays from anti-protonic hydrogen and deuterium, Nucl. Phys. **A483**, 631 (1988).

[18] M. Augsburger, D. Anagnostopoulos, G. Borchert, D. Chatellard, J.-P. Egger, P. El-Khoury, H. Gorke, D. Gotta, P. Hauser, P. Indelicato *et al.*, Measurement of the strong interaction parameters in antiprotonic deuterium, Phys. Lett. B **461**, 417 (1999).

[19] M. Augsburger, D. Anagnostopoulos, G. Borchert, D. Chatellard, J.-P. Egger, P. El-Khoury, H. Gorke, D. Gotta, P. Hauser, P. Indelicato *et al.*, Measurement of the strong interaction parameters in antiprotonic hydrogen and probable evidence for an interference with inner bremsstrahlung, Nucl. Phys. **A658**, 149 (1999).

[20] D. F. Phillips, M. A. Humphrey, E. M. Mattison, R. E. Stoner, R. F. C. Vessot, and R. L. Walsworth, Limit on Lorentz and CPT Violation of the proton using a hydrogen maser, Phys. Rev. D **63**, 111101 (2001).

[21] M. A. Humphrey, D. F. Phillips, E. M. Mattison, R. F. C. Vessot, R. E. Stoner, and R. L. Walsworth, Testing CPT and Lorentz symmetry with hydrogen masers, Phys. Rev. A **68**, 063807 (2003).

[22] R. M. Potvliege, A. Nicolson, M. P. A. Jones, and M. Spannowsky, Deuterium spectroscopy for enhanced bounds on physics beyond the standard model, Phys. Rev. A **108**, 052825 (2023).

[23] V. A. Kostelecký and A. J. Vargas, Lorentz and CPT tests with hydrogen, antihydrogen, and related systems, Phys. Rev. D **92**, 056002 (2015).

[24] A. J. Vargas, Prospects for testing CPT and Lorentz symmetry with deuterium ground-state Zeeman-hyperfine transitions, Phys. Rev. D **109**, 055001 (2024).

[25] I. I. Rabi, J. R. Zacharias, S. Millman, and P. Kusch, A new method of measuring nuclear magnetic moment, Phys. Rev. **53**, 318 (1938).

[26] D. Colladay and V. A. Kostelecký, CPT violation and the standard model, Phys. Rev. D **55**, 6760 (1997).

[27] D. Colladay and V. A. Kostelecký, Lorentz-violating extension of the standard model, Phys. Rev. D **58**, 116002 (1998).

[28] R. Bluhm, V. A. Kostelecký, and N. Russell, CPT and Lorentz tests in hydrogen and antihydrogen, Phys. Rev. Lett. **82**, 2254 (1999).

[29] G. Breit and I. I. Rabi, Measurement of nuclear spin, Phys. Rev. **38**, 2082 (1931).

[30] D. J. Wineland and N. F. Ramsey, Atomic Deuterium maser, Phys. Rev. A **5**, 821 (1972).

[31] P. J. Mohr, D. B. Newell, B. N. Taylor, and E. Tiesinga, Codata recommended values of the fundamental physical constants: 2022, Rev. Mod. Phys. **97**, 025002 (2025).

[32] V. A. Kostelecký and N. Russell, Data tables for Lorentz and CPT violation, Rev. Mod. Phys. **83**, 11 (2011).

[33] V. A. Kostelecký and M. Mewes, Electrodynamics with Lorentz-violating operators of arbitrary dimension, Phys. Rev. D **80**, 015020 (2009).

[34] V. A. Kostelecký and M. Mewes, Fermions with Lorentz-violating operators of arbitrary dimension, Phys. Rev. D **88**, 096006 (2013).

[35] V. A. Kostelecký and Z. Li, Gauge field theories with Lorentz-violating operators of arbitrary dimension, Phys. Rev. D **99**, 056016 (2019).

[36] V. A. Kostelecký and A. J. Vargas, Lorentz and CPT tests with clock-comparison experiments, Phys. Rev. D **98**, 036003 (2018).

[37] E. Widmann, R. Hayano, M. Hori, and T. Yamazaki, Measurement of the hyperfine structure of antihydrogen, Nucl. Instrum. Methods Phys. Res., Sect. B **214**, 31 (2004).

[38] M. Diermaier, C. Jepsen, B. Kolbinger, C. Malbrunot, O. Massiczek, C. Sauerzopf, M. Simon, J. Zmeskal, and E. Widmann, In-beam measurement of the hydrogen hyperfine splitting and prospects for antihydrogen spectroscopy, Nat. Commun. **8**, 1 (2017).

[39] C. Malbrunot, M. Diermaier, M. Simon, C. Amsler, S. Arguedas Cuendis, H. Breuker, C. Evans, M. Fleck, B. Kolbinger, A. Lanz *et al.*, A hydrogen beam to characterize the ASACUSA antihydrogen hyperfine spectrometer, Nucl. Instrum. Methods Phys. Res., Sect. A **935**, 110 (2019).

[40] L. Nowak, C. Malbrunot, M. Simon, C. Amsler, S. Arguedas Cuendis, S. Lahs, A. Lanz, A. Nanda, M. Wiesinger, T. Wolz *et al.*, CPT and Lorentz symmetry tests with hydrogen using a novel in-beam hyperfine spectroscopy method applicable to antihydrogen experiments, Phys. Lett. B **858**, 139012 (2024).

[41] See Supplemental Material at http://link.aps.org/supplemental/10.1103/dqvd-15q4 for details on beam path Sec. A.1, which includes Ref. [42], details on oscillating magnetic field Sec. A.2, which includes Refs. [43–45], details on static magnetic field Sec. A.3, which includes Ref. [45], details on data acquisition protocol Sec. B, and for an example and a comprehensive table on SME constraints Sec. C, which includes Refs. [20,23,24].

[42] https://e-opthos.com/microwave-cavities.

[43] M. W. Reynolds, M. E. Hayden, and W. N. Hardy, Hyperfine resonance of atomic deuterium at 1 K, J. Low Temp. Phys. **84**, 87 (1991).

[44] https://cubicure.com/en/hot-lithography/.

[45] COMSOL Multiphysics, https://www.comsol.com.

[46] G. Özşahin, T. Şimşek, M. Ünlü, O. Kiriş, S. Köse, H. Mustaçoğlu, F. Öztürk, and V. Akan, Parametric analysis of double-split ring resonator as a reflectarray unit cell, in *2017 IEEE International Symposium on Antennas and Propagation & USNC/URSI National Radio Science Meeting* (IEEE, Piscataway, 2017), pp. 101–102.

[47] C. Debus and P. H. Bolivar, Frequency selective surfaces for high sensitivity terahertz sensing, Appl. Phys. Lett. **91**, 184102 (2007).

[48] N. Kaur, F. Frank, J. Pinto, P. Tuckey, and P.-E. Pottie, A 500-km cascaded white rabbit link for high-performance frequency dissemination, IEEE Trans. Ultrason. Ferroelectr. Freq. Control **69**, 892 (2022).

[49] E. Cantin, M. Tønnes, R. L. Targat, A. Amy-Klein, O. Lopez, and P.-E. Pottie, An accurate and robust metrological network for coherent optical frequency Dissemination, New J. Phys. **23**, 053027 (2021).

[50] https://www.refimeve.fr/index.php/en/.

[51] The theoretical analysis toward the present experiment [24] assumes $\vartheta \simeq 49^\circ$ corresponding to the opposite magnetic field direction than applied in this work.

[52] C. Killian, Z. Burkley, P. Blumer, P. Crivelli, F. P. Gustafsson, O. Hanski, A. Nanda, F. Nez, V. Nesvizhevsky, S. Reynaud *et al.*, GRASIAN: towards the first Demonstration of gravitational quantum states of atoms with a cryogenic hydrogen beam, Eur. Phys. J. D **77**, 50 (2023).

[53] C. Killian, P. Blumer, P. Crivelli, O. Hanski, D. Kloppenburg, F. Nez, V. Nesvizhevsky, S. Reynaud, K. Schreiner, M. Simon *et al.*, GRASIAN: shaping and characterization of the cold hydrogen and deuterium beams for the forthcoming first demonstration of gravitational quantum states of atoms, Eur. Phys. J. D **78**, 132 (2024).

[54] N. F. Ramsey, A molecular beam resonance method with separated oscillating fields, Phys. Rev. **78**, 695 (1950).

[55] N. F. Ramsey, Experiments with separated oscillatory fields and hydrogen masers, Rev. Mod. Phys. **62**, 541 (1990).

[56] A. Nanda, Progress towards ramsey hyperfine spectroscopy in asacusa, in *CPT and Lorentz Symmetry* (World Scientific, Singapore, 2020), pp. 201–203.

[57] T. Schmidt, Über die magnetischen Momente der Atomkerne, Z. Phys. **106**, 358 (1937).

[58] J. T. VanderPlas, Understanding the Lomb–Scargle periodogram, Astrophys. J. Suppl. Ser. **236**, 16 (2018).

[59] J. T. VanderPlas and Željko Ivezić,Periodograms for multiband astronomical time series, Astrophys. J. **812**, 18 (2015).

[60] J. Vanderplas, A. J. Connolly, Željko Ivezić, and A. G. Gray, Introduction to astroML: Machine learning for astrophysics, in *2012 Conference on Intelligent Data Understanding*, vol. 47 (2012).

[61] N. R. Lomb, Least-squares frequency analysis of unequally spaced data, Astrophys. Space Sci. **39**, 447 (1976).

[62] J. D. Scargle,Studies in astronomical time series analysis. II. Statistical aspects of spectral analysis of unevenly spaced data, Astrophys. J. **263**, 835 (1982).

[63] A. M. Price-Whelan, P. L. Lim, N. Earl, N. Starkman, L. Bradley, D. L. Shupe, A. A. Patil, L. Corrales, C. E. Brasseur *et al.* (Astropy Collaboration), The Astropy project: Sustaining and growing a community-oriented open-source project and the latest major release (v5.0) of the core package, Astrophys. J. **935**, 167 (2022).

[64] A. M. Price-Whelan, B. M. Sipőcz, H. M. Günther, P. L. Lim, S. M. Crawford, S. Conseil, D. L. Shupe, M. W. Craig, N. Dencheva *et al.* (Astropy Collaboration), The Astropy project: Building an open-science project and status of the v2.0 core package, Astron. J. **156**, 123 (2018).

[65] T. P. Robitaille, E. J. Tollerud, P. Greenfield, M. Droettboom, E. Bray, T. Aldcroft, M. Davis, A. Ginsburg, A. M. Price-Whelan *et al.* (Astropy Collaboration), Astropy: A community python package for astronomy, Astron. Astrophys. **558**, A33 (2013).

[66] L. S. Dreissen, C.-H. Yeh, H. A. Fürst, K. C. Grensemann, and T. E. Mehlstäubler, Improved bounds on Lorentz violation from composite pulse Ramsey spectroscopy in a trapped ion, Nat. Commun. **13**, 7314 (2022).

[67] R. V. Baluev, Assessing the statistical significance of periodogram peaks, Mon. Not. R. Astron. Soc. **385**, 1279 (2008).

End Matter

SME sensitivity of other experiments—High precision comagnetometry experiments employ even-odd noble gases. Direct sensitivity to n related SME coefficients originates from the valence neutron, while sensitivity to p coefficients is suppressed. So far only the Schmidt model [57] has been applied to the respective heavier nuclei in context of the SME framework. In this model nucleons are paired to form states of zero total angular momentum, which results in a complete insensitivity of comagnetometry experiments to p coefficients [36]. This model-dependent situation could change in the future if a residual sensitivity to SME p coefficients was quantified by more sophisticated nuclear structure modelling within the SME framework.

Empirical fit function—In the present Letter, the hyperfine transition frequency is the quantity that is tested for variations during a sidereal day. A line shape fit retrieves a value for the central transition frequency ν^c from the observed resonance spectra as a proxy for the true value ν^c_{true}. Understanding the physics behind the observed line shape in detail is useful but not critical. For instance, a constant systematic offset $\Delta\nu_{\text{syst}} = \nu^c - \nu^c_{\text{true}}$ is of minor concern in a search for variations.

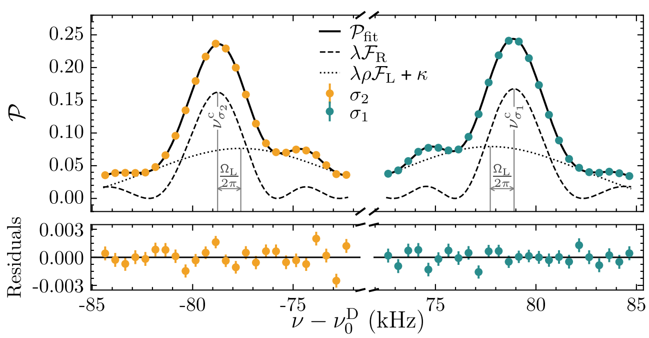

FIG. 5. Campaign No. 1 equivalent of Fig. 3. Dashed and dotted lines show Rabi- and Lorentz-type contributions to the empirical fit function given by Eq. (B2).

Consequently, it is sufficient to apply an empirical fit function.

Our Rabi-type spectroscopy measures the reduction in beam rate while a stimulating rf field becomes resonant with the transition of interest. The drop in rate depends on the applied rf frequency ν and is proportional to the transition probability $\mathcal{F}_{\text{R}}$ ideally given by

$$\mathcal{F}_{\text{R}}(\nu;\nu^c,\Omega_{\text{R}},\tau_{\text{int}}) = \frac{\sin^2\left(\frac{\Omega_{\text{R}}\tau_{\text{int}}}{2}\sqrt{1+\left(\frac{\Delta\Omega}{\Omega_{\text{R}}}\right)^2}\right)}{1+\left(\frac{\Delta\Omega}{\Omega_{\text{R}}}\right)^2}. \quad \text{(B1)}$$

The Rabi frequency Ω_{R} quantifies the constant interaction strength. $\Delta\Omega = 2\pi(\nu-\nu^c)$ is the detune replacing the scan variable ν and the parameter ν^c on the right-hand side of the equation. On resonance ($\Delta\Omega = 0$), the first population inversion is achieved when the condition for a π pulse is satisfied: $\Omega_{\text{R}}\tau_{\text{int}} = \pi$. In the present experiment τ_{int} is given by the velocity of the D atoms and the length of the interaction apparatus and amounts to ~400 μs. The Rabi frequency can be optimized to a π pulse by adjusting the rf power P_{rf} applied to the cavity due to the proportionalities $\Omega_{\text{R}} \propto B_{\text{osc}} \propto \sqrt{P_{\text{rf}}}$.

Distortions of the line shape are caused by imperfections. The following empirical modifications are made to Eq. (B1) to account for those. The Rabi-type line shape is extended by an asymmetry parameter ξ, which enters by rewriting $\Delta\Omega/\Omega_{\text{R}} \to \Delta\Omega/(\Omega_{\text{R}}+\xi\Delta\Omega)$. Furthermore, a Lorentzian background is added: $\mathcal{F}_{\text{L}} = \{1+[(\Delta\Omega+\Omega_{\text{L}})/\Gamma]^2\}^{-1}$, with a width Γ and a frequency-offset Ω_{L}. $\mathcal{F}_{\text{R}}$ and $\mathcal{F}_{\text{L}}$ are combined with a weighing factor ρ on the Lorentz contribution and then scaled to the directly measured probability ($\mathcal{P}_{\text{meas}} = 1 - R_\sigma/\bar{R}_{\text{ref}}$, compare main text) by a multiplier λ and constant offset κ. Hence, the resulting empirical probability fit-function has 9 parameters:

TABLE III. Values with single standard deviations of six predetermined parameters of the empirical fit function (B2) obtained from fits to the high-statistic average spectra of each σ transition and campaign, as shown in Figs. 3 and 5. In the final fits of resonance pairs, these six predetermined parameters are fixed to the mean values shown in the last column, leaving only three free parameters (ν^c, λ, κ).

Parameter			Campaign No. 1		Campaign No. 2		
Name	Symbol	Units	σ_1	σ_2	σ_1	σ_2	Mean
Rabi asymmetry	ξ	1	0.0423(22)	−0.0402(23)	0.0329(32)	−0.0323(32)	±0.0384
Rabi frequency	Ω_{R}	rad ms^{-1}	11.07(22)	11.05(22)	9.62(43)	9.87(38)	10.77
Interaction time	τ_{int}	ms	0.2758(13)	0.2753(14)	0.2793(22)	0.2808(22)	0.2768
Lorentz probability ratio	ρ	1	0.913(56)	0.865(57)	0.740(44)	0.823(53)	0.822
Lorentz frequency offset	Ω_{L}	rad ms^{-1}	7.44(16)	−7.25(16)	6.60(22)	−6.15(19)	±6.96
Lorentz width	Γ	rad ms^{-1}	51.6(25)	49.8(27)	37.0(19)	41.3(26)	43.5

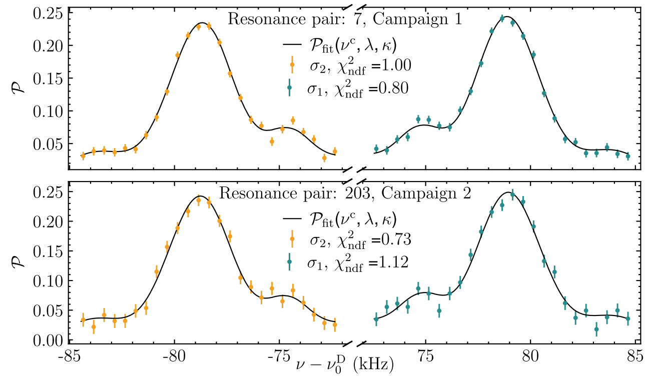

FIG. 6. Examples of three-parameter fits to single resonance pairs from campaign No. 1 and No. 2 including typical values for reduced squared residuals ($\chi^2_{\rm ndf}$).

$$\mathcal{P}_{\rm fit}(\nu;\nu^{\rm c},\lambda,\kappa,\xi,\Omega_{\rm R},\tau_{\rm int},\rho,\Omega_{\rm L},\Gamma)$$
$$=\lambda[\mathcal{F}_{\rm R}(\Delta\Omega;\xi,\Omega_{\rm R},\tau_{\rm int})+\rho\mathcal{F}_{\rm L}(\Delta\Omega;\Omega_{\rm L},\Gamma)]+\kappa. \quad \text{(B2)}$$

In Fig. 5, the Rabi and Lorentz part of the fit function are illustrated. The parameters $\xi, \Omega_{\rm R}, \tau_{\rm int}, \rho, \Omega_{\rm L}$, and Γ are predetermined by fits to high-statistic spectra, which are obtained by averaging all spectra of each campaign for both σ transitions. The values are summarized in Table III. A quantitative interpretation of Rabi-type line shape parameters is not meaningful, as the Lorentz-type background is introduced *ad hoc*. The parameters ξ and $\Omega_{\rm L}$ control asymmetries. Therefore they are sign-opposite for the σ_1 and σ_2 transitions as their line shapes are mirrored due to sign-opposite Zeeman shifts. Deviations between parameters for the two resonances of the same campaign are within uncertainties, while tensions exist between the campaigns. Slight changes of static and rf field properties in combination with correlation between fit parameters can explain those. The final analysis applies the empirical function with only three open fit parameters ($\nu^{\rm c},\lambda,\kappa$) and the other six predetermined parameters fixed to the mean values tabulated in the last column of Table III. Examples of this three-parameter fit are illustrated in Fig. 6 for resonance pairs of each campaign. The use of the parameter values of either campaign No. 1 or No. 2 produces the same results for the complex amplitudes within 5% of the statistical uncertainty.

TABLE IV. Comparison of frequency averages $\overline{\nu^{\rm c}_\pm}$ for groups of data (No. 1a, No. 1b, No. 2). The top row states the respective number of acquired resonance pairs. Uncertainties are single standard deviations.

Campaign:	No. 1a	No. 1b	No. 2	Joint
Acqu. res. pairs:	82	24	107	213
$(\overline{\nu^{\rm c}_-}-157\,000)$ Hz:	699 ± 5	668 ± 10	739 ± 6	709.1 ± 3.5
$(\overline{\nu^{\rm c}_+}-2\nu_0^{\rm D})$ Hz:	157 ± 5	136 ± 10	163 ± 6	156.6 ± 3.5

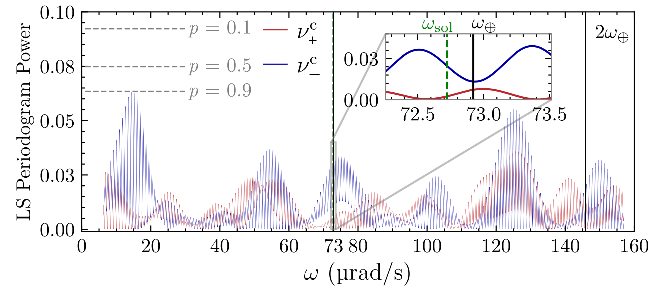

FIG. 7. The graph shows standard normalized Lomb-Scargle periodograms for $\nu^{\rm c}_\pm$ with horizontal dashed lines indicating p values (details see text). The inset zooms into the frequency region of the sidereal and solar day.

Systematics, offset corrections, data groups—In spite of using the same current set values, the magnetic field was not identical in the two campaigns separated by three months. In addition, a malfunction of the high-precision current supply after 82 out of 106 resonance pairs of campaign No. 1 required a reset. Therefore, the complex amplitudes $\mathcal{A}_1^-$, $\mathcal{A}_1^+$, and $\mathcal{A}_2^+$ are extracted after offset corrections on $\nu^{\rm c}_\pm$ with three distinct frequency averages referred to as No. 1a, No. 1b, and No. 2 in Table IV. The complex amplitudes shift slightly when the offset correction is performed with a single joint frequency average instead (last column of Table IV). The absolute difference $|\mathcal{A}^{\rm indiv.}-\mathcal{A}^{\rm joint}|$ yields the systematic errors listed in the last row of Table I.

Lomb-Scargle periodograms—The presence of other frequency components in the time evolution of $\nu^{\rm c}_\pm$ was tested by a Fourier transform method for unevenly sampled time series referred to as Lomb-Scargle periodograms [58–62]. Widely used by the astrophysics communities [63–65], the method has been recently applied in searches for sidereal variations to constrain Lorentz violations [66]. The periodogram of the combined frequencies $\nu^{\rm c}_\pm$ are shown in Fig. 7. The frequency $\nu^{\rm c}_-$ is more sensitive to changes of $B_{\rm stat}$ that could be induced by environmental fluctuations, therefore the observation of higher power values in comparison to $\nu^{\rm c}_+$ is reasonable. Even the highest observed power levels can be explained with $\geq 90\%$ probability as Gaussian noise when interpreted as p values using the methods developed by Baluev [67]. The inset zooms onto the frequency region of interest. The small fringes appear due to the three-month time separation between the two campaigns. Day-night effects can thus be resolved from sidereal variations.